The processing route towards outstanding performance of the severely deformed Al-Mg-Mn-Sc-Zr alloy

Elena Avtokratova[a], Oleg Sitdikov[a], Michael Markushev[a], Michael Linderov[b], Dmitry Merson[b] and Alexey Vinogradov[c*]

[a] Institute for Metals Superplasticity Problems RAS, 39 Khalturin St., Ufa, Russia
[b] Institute of Advanced Technologies, Togliatti State University, Togliatti, Russia
[c] Department of Mechanical and Industrial Engineering, Norwegian University of Science and Technology-NTNU, N-7491 Trondheim, Norway

*Corresponding author: E-mail alexei.vinogradov@ntnu.no

Abstract: Aiming at obtaining the enhanced mechanical properties profile for lightweight applications, bulk billets of the commercial 1570C aluminium alloy (Al-5Mg-0.18Mn-0.20Sc-0.08Zr, wt. %) with nanosized aluminides of transition metals (TM) were subjected to various thermomechanical treatments comprising severe plastic deformation for grain refinement and favourable distribution of disperse phases. The potential of multiaxial isothermal forging (MIF) for the fabrication of ultrafine-grain advanced aluminium alloys is unveiled via a multistep pathway involving two primary routes – the one under constant processing temperature and the other with the inter-step temperature reduction from 325 to 175°C - combined with conventional cold rolling or high-pressure torsion. Processing-dependent microstructural factors controlling the alloy's behaviour under monotonic and cyclic loading at ambient temperature are discussed with the account of the role of the grain size, grain boundary distribution, precipitates of Mg-rich β-phase and TM-aluminides. In particular, it is shown that after MIF followed by cold rolling, the outstanding combination of the tensile strength and ductility was observed concomitantly with the fatigue resistance superior to that in the contemporary alloys of the same class and/or of many currently available commercial high-strength alloys.

Keywords: aluminium alloys; multiaxial isothermal forging; nanostructure; precipitates; mechanical properties; fatigue

1. Introduction

The non-heat-treatable aluminium-magnesium alloys with complex additions of transition metals (TM) constitute a modern class of commercial lightweight materials with the unique balance between weight, mechanical performance, corrosion resistance, weldability, etc. [1,2]. The exceptional property profile is obtained in this class of structural alloys thought the simultaneous control and application of thermal and deformation processing applied to the initial as-cast material. The conventional thermomechanical processing (TMP) designed for non-heat-treatable alloys rely primarily upon solid solution strengthening and strain hardening controlled for the favourable combination of strength and ductility that is achieved predominantly due to the tailored dislocation arrangement and density. The alternative approach towards developing new materials with enhanced properties and improved performance is footed on the methodology combining grain refinement and grain boundary design. In this way, ultrafine grain (UFG) or even nanocrystalline structures (having the grain size less than 1 and 0.1 µm, respectively) are fabricated under conditions permitting the control over the distribution of grain boundary misorientation angles [3-5]. This approach has been proven particularly useful for the alloys with complex additions of TMs [6] where profuse precipitation of TM aluminides (so-called dispersoids) occurs during the heat treatment and the following-up hot deformation procedure resulting in the greatly refined microstructure. Facilitating grain refinement and stabilising the deformation microstructure, dispersoids also play an essential role as strengthening agents, enabling particle hardening of the aluminium-based solid solution matrix [1].

In the recent decade, it has been frequently shown that ultimate properties improvement can be achieved in Al-alloys through nanostructuring via TMP involving severe plastic deformation (SPD) which are capable of imposing giant strains e>>1 on workpieces [3-5]. One of the key advantages of SPD techniques is their ability to combine the effect of strain hardening with other major strengthening mechanisms - Hall-Petch, solid solution and disperse hardening - in a single processing route. Along with the control over the microstructure components including the grain/subgrain size and shape, the volume fraction of recrystallised grains, distributions of grain boundary types and angles of misorientation, SPD enables varying the dimensions, fractions and distributions of the second phases including both coarse excess phases and fine precipitates.

Amongst many SPD techniques devised to produce bulk nanostructured materials [5], the historically first and, admittedly, the most popular method capable of extreme grain refinement is known as high-pressure torsion (HPT). It is frequently applied to disk-shaped samples and performed up to several tens of rotations under several GPa pressure at ambient temperature, giving rise to grain size reduction down to a few ten nanometres in a wide variety of pure metals and alloys [7-9]. However, the dimensions of the processed samples are usually far too small for any engineering application. Another widespread technique is known as equal-channel angular pressing (ECAP) whereby simple shear is applied to a working billet during multiple passages through intersecting channels with a constant cross-section. This process also faces upscaling challenges to be overcome for broader uptake by industry [10-12]. The affordable, yet versatile, SPD technique is known as multistep isothermal forging (MIF). This process can be easily combined with rolling or other metal forming operations, enabling mass productions of rods, plates and sheets [13].

Fatigue properties are often pivotal for prospective applications. Unlike the spectacular improvement in monotonic strength after SPD, which has triggered boosted research in the field, the fatigue properties are notoriously more difficult to control and improve by deformation processing for several reasons. While discussing the structure-property relationships, the correlations are most frequently emphasised between average microstructural characteristics (such as mean grain size) and average mechanical properties (such as yield stress assessed in monotonic loading) [14,15]. On the other hand, the fatigue properties can be regarded as those limited by the "weakest link" existing in the microstructure, depending not only on the average structural parameters, but rather, and mostly, on their distributions and extreme values such as the largest grain size, largest non-metallic inclusion diameter or peak values of internal stresses around local stress risers, severe strain gradients and microcracks, which can be induced during TMP. Besides, the wavy-slip metals and alloys tending to form the low-angle cellular dislocation structures do not exhibit a strong grain-size dependence until the grain size is reduced below the typical cell size [16-18]. This applies to many SPD processed fcc metals including Al-alloys (e.g. the non-heat-treatable alloy 5056 [19,20]). The capacity of SPD to mitigate the conventional strength-ductility trade-off has been well-documented for Al-based alloys with grain/subgrain refinement below 1 μm [21-24]. This, in turn, results in appreciable enhancement of both low- and high-cyclic fatigue properties [25,26]. However, for the complex alloy systems, including the majority of aluminium alloys containing TM, the effect of SPD processing on the microstructure and properties is notably less obvious.

Transition metals like Mn, Cr, Zr, Sc are fabulous additions to commercial Al alloys as they have long been recognised as strong modifiers of the cast microstructure [27]. Among them, Zr and Sc are known as the most effective hardening agents, forming high densities of coherent nanosized dispersoids, e.g. $Al_3Zr(Sc)$ [28]. Thereby, they exert a strong effect on virtually all properties of aluminium alloys, giving rise to a remarkable enhancement in strength-ductility synergy, corrosion resistance, thermal stability and superplastic behaviour [1,29-31]. All these properties can be further improved by SPD via HPT [32,33], ECAP [34], twist extrusion [35] or a combination of ECAP with cold rolling [36], etc. The fatigue properties of Al-Mg-TM alloys, especially with Sc additions, have been only scarcely studied [32-34, 37-40] and need to be updated.

The present study is aimed at addressing two primarily issues: (i) exploring the limits of improving the mechanical properties of the complex Al-Mg-Mn-Sc-Zr alloy via thermomechanical processing via SPD involving a combination of MIF with conventional cold rolling (CR) and/or HPT, and (ii) getting a more in-depth insight into understanding the structure-property relations with the emphasis placed on the role of grain structure and secondary phases in the mechanical response in general and the fatigue resistance in particular.

2. Material and Testing

The commercial 1570C alloy ingots with the nominal chemical composition of Al-5Mg-0.18Mn-0.20Sc-0.08Zr (in wt. %) were homogenised in air at 360°C for 6 hours (further designated as the as-cast condition). Rods of ⌀80×150 mm were cut from an ingot and MIF processed via two different routes. The first one (designated as MIF1) comprised of 12 deformation cycles performed at 325°C with the cumulative equivalent strain e of 12. Each deformation cycle included several consecutive settings and drawings of a billet to maintain its shape and

dimensions close to the initial ones (see [7,13] for more details). The second route involved the MIF1 followed by two additional deformation stages performed at 250 and 175°C, respectively, with e of 6 on each step and designated as MIF3 (with the total effective strain e=24). Herewith, we have tested two main MIF routes – multidirectional isothermal forging under constant and decreased temperature conditions. After homogenisation and forging, the samples were water-cooled.

CR to a total strain of e~1.6 was performed at ambient temperature on 10 mm thick plates cut from the MIF1 processed billet. The disk-shaped samples of 20 mm diameter and 2 mm thick cut from the same billet, were also severely strained via HPT carried out to 10 revolutions under 6 GPa pressure at room temperature.

The alloy microstructure was examined by optical, transmission and scanning electron microscopy (OM Nikon L-150, TEM JEOL-2000EX and SEM TESCAN MIRA 3 LMH FEG equipped with the Oxford Instruments HKL Channel 5 EBSD system, respectively) and the X-ray diffraction (XRD, DRON-7) analysis. The average misorientation angle between grains/subgrains, Θ_{ave} and the fraction of high angle boundaries (HABs) (with $\Theta \geq 15°$), f_{HABs}, were determined using the SEM-EBSD data.

The average size of grains and subgrains was measured by the SEM·EBSD technique and/or the analyses of TEM images using the circle equivalent diameter method. The size and density of dispersoids were assessed by the digital analysis of the dark-field TEM images with not less than 2000 precipitates measured. The average size of precipitates was evaluated by measuring their diameter. The phase number density was measured as a ratio of the number of precipitates per unit of the TEM image area and the thickness of a foil. The latter was evaluated by the extinction contours appearing at the grain boundaries. Besides, a combination of scanning transmission electron microscopy (STEM) and energy-dispersive spectroscopy (EDS) was used to assess the composition of intermetallic phases. For OM analysis, the mechanically pre-polished samples were etched in a Keller's reagent. The samples for SEM and TEM investigations were prepared by mechanical grinding and polishing, and finally electro-polished in a 20% nitric acid solution in methanol at -28°C.

The Vickers microhardness was measured at 0.5 and 1N loads applied for 10 sec using the ITV-1-M microhardness tester. The tensile and fatigue tests were performed on Instron 1182 and E1000 machines, respectively, at ambient temperature. The flat specimens were shaped by spark erosion and mechanically polished to a mirror-like finish. The tensile properties - the 0.2% yield stress, ultimate tensile strength and elongation to failure - were determined as an average of 3-8 measurements made at the nominal strain rate of 2×10^{-3} s^{-1}. The dog-bone shape specimens had a gage part of $1.5 \times 3 \times 6$ mm^3 for the as-cast, MIF1, MIF3 and MIF1+CR conditions, and $1 \times 1 \times 3$ mm^3 for MIF1+HPT. In the former case, the specimens were cut along the last drawing/rolling direction, while in the latter case the specimen longitudinal axis coincided with the tangent to the circle at the half-radius of the deformed discs. To characterise the fatigue resistance in the stress-controlled cyclic testing, the hourglass shape samples with a minimum cross-section of 1×0.9 mm^2 were tested in the repeated tension mode at the constant stress amplitude σ_a with the stress ratio R = $\sigma_{max}/\sigma_{min}$=0.1 and 60 Hz frequency (with σ_{max} and σ_{min} denoting the maximum and minimum stress per cycle, respectively).

3. Results and Discussions

3.1. Microstructure

The OM, SEM and TEM observations have shown that, after homogenisation, the microstructure of the aluminium matrix was comprised of equiaxial grains with an average size of 25 μm and grain boundary distribution exhibiting preferably high-angle misorientations (Fig. 1a-c). Under annealing, the solid solution, which had been abnormally supersaturated by TMs, decomposed and $Al_3(Sc,Zr)$ compact precipitates were formed with a diameter of about 10-15 nm and density of 1×10^4 μm^{-3} (Fig. 2a,b). One can notice that the strong refection spots in the selected electron diffraction pattern due to the Al-matrix are clearly visible, while fine spots of $Al_3(Sc,Zr)$ precipitates appear at around 1/2-typed positions being halfway between strong reflections. This suggests that the precipitates are fully coherent with the matrix [41, 42]. Also, their coherency with the matrix was testified by the coffee-bean contrast [41] visible in the bright-field TEM images taken at higher magnification (see the enlarged fragment in Fig. 2a). The density of precipitates across the billet and inside the grains was relatively uniform (Fig. 2a,b) and their size distribution was unimodal (Fig. 2c). The grain boundary precipitate-free zones (PFZs) (Fig. 2d) with only much coarser Sc-rich separate precipitates[1] (Fig. 2e,f) were frequently observed in a way similar to those commonly seen in age-hardened alloys [44]. These PFZs are softer compared to grain interiors, thus being preferred sites for strain localisation and fracture initiation under monotonic and cyclic loads.

During the first MIF cycles, the new fine subgrains and grains surrounded by low- and high-angle boundaries were formed in the vicinity of initial grain boundaries [3, 45]. As the deformation proceeds, the fraction and misorientation of these grains increased, leading to a gradual replacement of the initial coarse-grain structure by the fine-grain one (Figs. 1d-f and 3a,d). The primary grain refinement mechanism was continuous dynamic recrystallisation occurring via a progressive conversion of low-misoriented subgrains into grains bounded by a mixture of low- and high-angle grain boundaries. It has been well understood that this process is controlled by the interaction of lattice dislocations and (sub)grain boundaries with dispersoids impeding boundary migration and grain growth [3,6,45]. The recrystallisation process was inevitably accompanied by the rearrangement of dislocations and dynamic recovery in the matrix. However, until the end of the first MIF stage, the matrix appeared partially recrystallised with of 1.8-2.0 μm subgrains inside the fragments of initial grains surrounded by slightly coarser new grains of 2.2 μm in diameter (Fig. 1d-f).

After the MIF3 route, the microstructure appeared more refined and homogeneous (Fig. 1g-i and 3b,e). The grains and subgrains reduced to ~1 μm. The TEM images reveal that the majority of grain boundaries are featured by the non-uniform extinction contrast. The increased density of dislocations was also evident in TEM images. These findings indicate that with the decreasing forging temperature, the alloy's microstructure became less equilibrium.

---

[1] This suggests that some intense coarsening of aluminides took place in the grain boundary region. The most common reasons for that can be the higher diffusion rate of dissolved atoms of Sc (Zr) along the high-angle boundaries, if compared to that in the grain bodies [6]. It may also be suggested that the clusters/chains of coarser particles as well as fan-shaped zones of particle aggregations represented in Fig. 2 d-f are the result of activity of another precipitation mechanism (e.g. discontinuous precipitation) operated in the grain boundary region during homogenisation, as described elsewhere [43]. The observation of interspersed Sc-rich (point 1) and Sc-depleted (point 2) areas in fan-shaped aggregation zone in Fig. 2e supports this assumption.
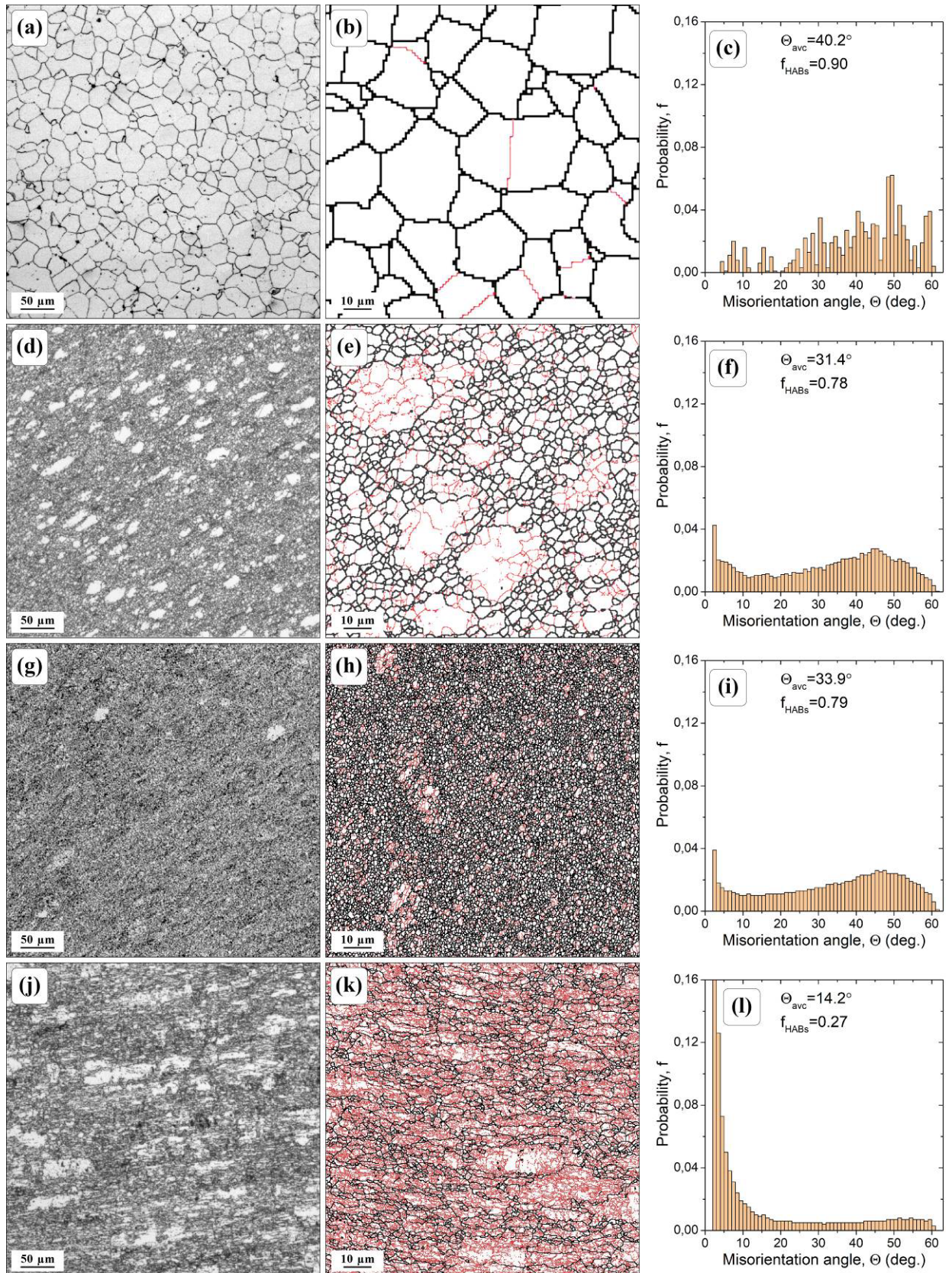
Figure 1. Optical microscopy (a,d,g,j) and SEM-EBSD (b,e,h,k) images representing typical grain structure and grain-boundary distributions (c,f,i,l) in the alloy 1570C after homogenisation (a-c), MIF1 (d-f), MIF3 (g-i) and MIF1+CR (j-l) processing. Low- (2°≤Θ<15°) and high-angle (Θ≥15°) boundaries are highlighted on the EBSD maps by black and red lines, respectively.

The XRD peak profile analysis (the corresponding X-ray diffraction patterns are represented in the Supplementary Materials, Fig. S1) revealed the almost one order increase in the total dislocation density and the twice higher residual stresses (Table 1), which are caused by the more significant suppression of the dynamic recovery. Besides, processing at temperatures below the solvus point (~250°C) resulted in the formation (in addition to TM aluminides) of a rather coarse (50–500 nm) β-phase (Al-Mg) precipitates inside the crystallites and along their boundaries (Fig. 3e) (interested readers may review also the STEM image and the distribution maps of primary elements - Al and Mg - presented in Supplementary Materials, Fig. S2).

During cold rolling of the MIF1-processed alloy, the fine-grain microstructure transformed into the severely work-hardened one featured by the high dislocation densities and the prevalence of low-angle boundaries (Figs. 1j-l and 3c,f). This structure can be regarded as cellular. The cell size is found to be three-five times lesser than the grain size, still being far over the nano-range.
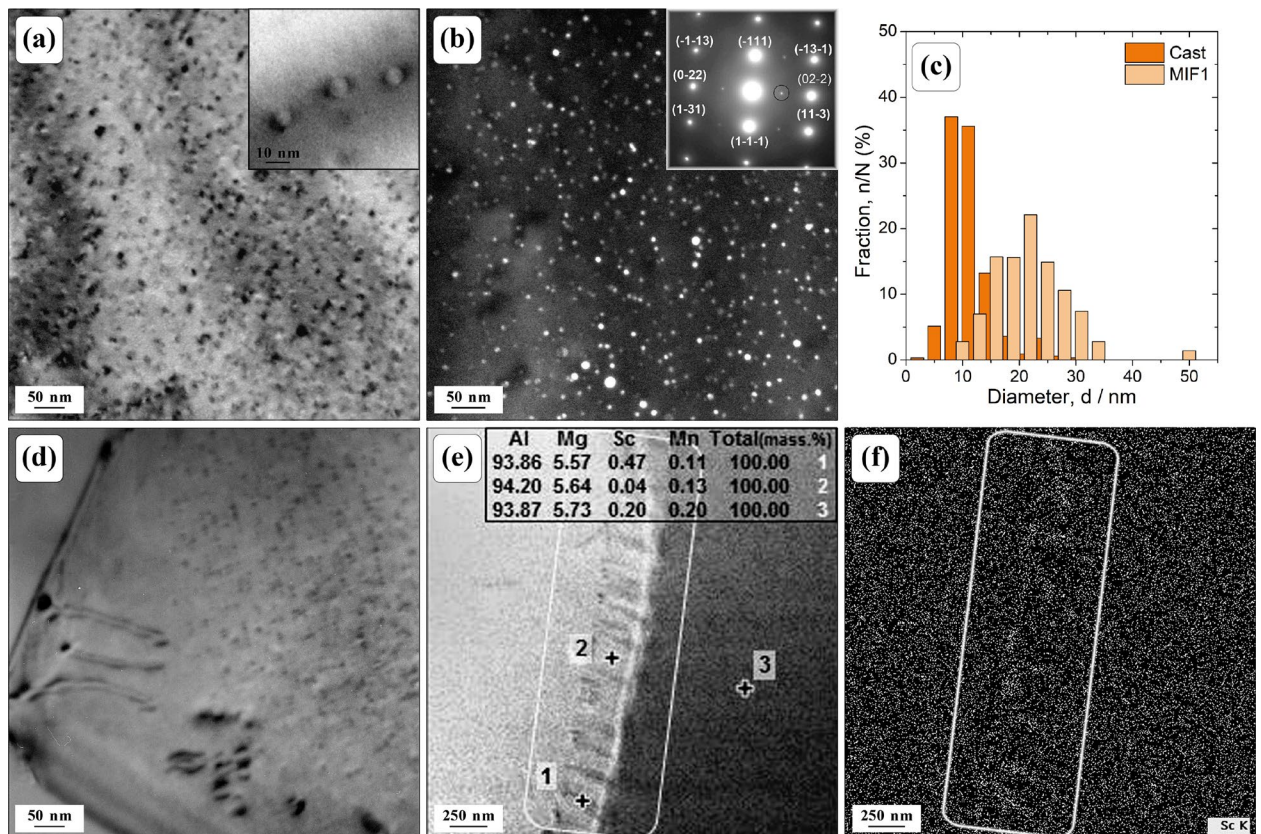

Figure 2. TEM images of the Al$_3$(Sc,Zr) precipitates in the homogenised billet of the alloy 1570C: bright-(a) and dark-field TEM images in Al$_3$(Sc,Zr) refection, indicated in selected area diffraction pattern shown in the inset (zone axis <211>) (b); and their size distribution before and after MIF1 (c); typical TEM image of the grain boundary region with the non-homogeneous distribution of precipitates (d); STEM-EDS image and corresponding chemical compositions taken at points 1 and 2 in the close proximity to the grain boundary in the fan-shaped zones of particle aggregations and at point 3 in the grain interior (e), and the microprobe Sc map (f) corresponding to (e).
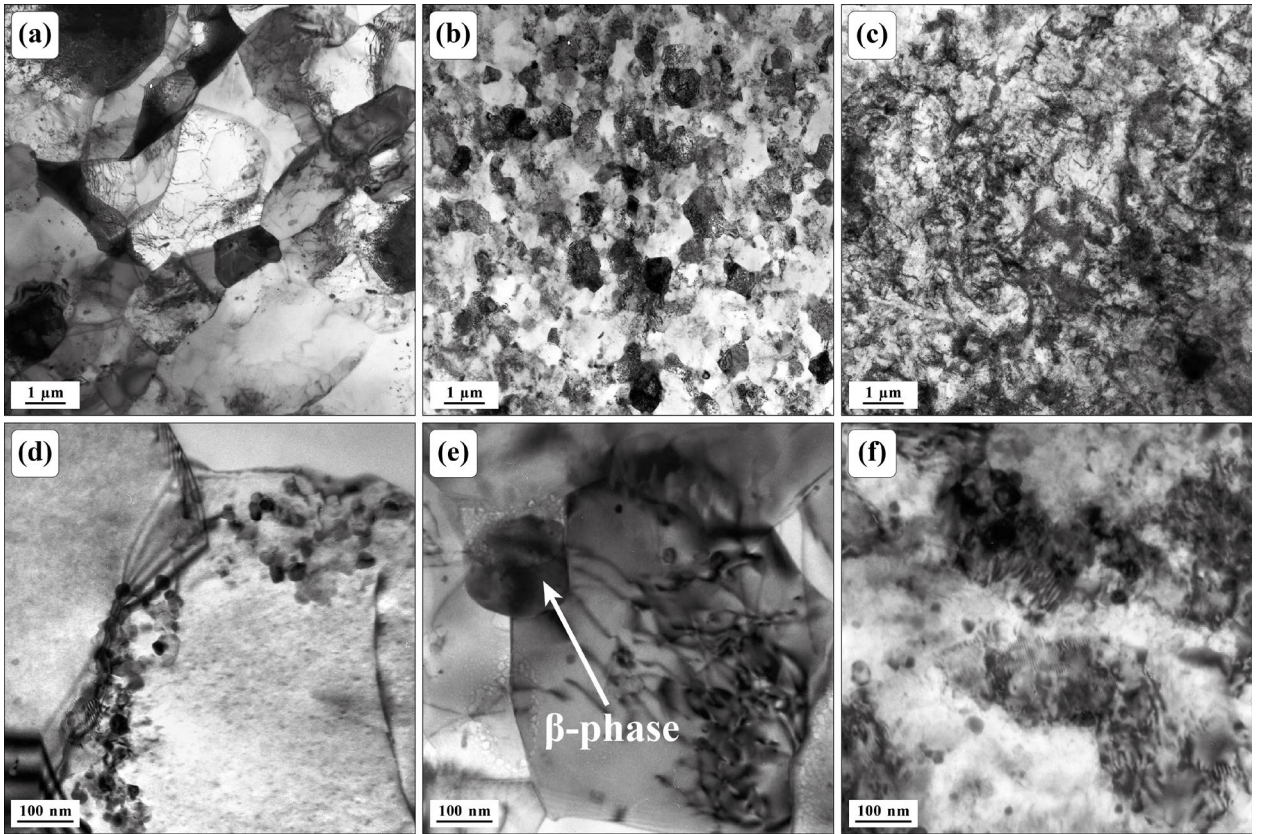
Figure 3. Typical TEM structures of the alloy 1570C after MIF1 (a,d), MIF3 (b,e) and MIF1+CR (c,f)

Table 1. X-ray data of the aluminium matrix of the 1570C alloy.

Condition	Lattice Parameter, Å	Coherent Domain Size, nm	$<\varepsilon^2>^{1/2}$, %	Dislocation Density, m^{-2}
As-cast	4.074±0.001	1116±100	0.035±0.001	$5×10^{12}$
MIF1	4.068±0.001	688±12	0.032±0.003	$5×10^{12}$
MIF3	4.060±0.001	197±13	0.073±0.002	$5×10^{13}$
MIF1+CR	4.066±0.001	59±5	0.163±0.002	$3×10^{14}$
MIF1+HPT	4.061±0.001	73±5	0.121±0.003	$2×10^{14}$

Unlike cold–rolling, HPT transformed the initial fine-grain structure into the ultimately deformed non-equilibrium nanostructure consisting primarily of nanosized fragments represented by predominantly equiaxed crystallites of 150 nm in diameter (Fig. 4). Concurrently, the coherent domain size reduced by a factor of 9 from the original 690 nm measured in the MIF1 state (Table 1). Similar microstructures are commonly found in HPT processed aluminium alloys [46]. As opposes to other deformation structures investigated in the present study (excluding the CR-processed one) MIF1+HPT treated specimens are characterised by high dislocation densities and high residual stresses (Fig. 4 and Table 1).
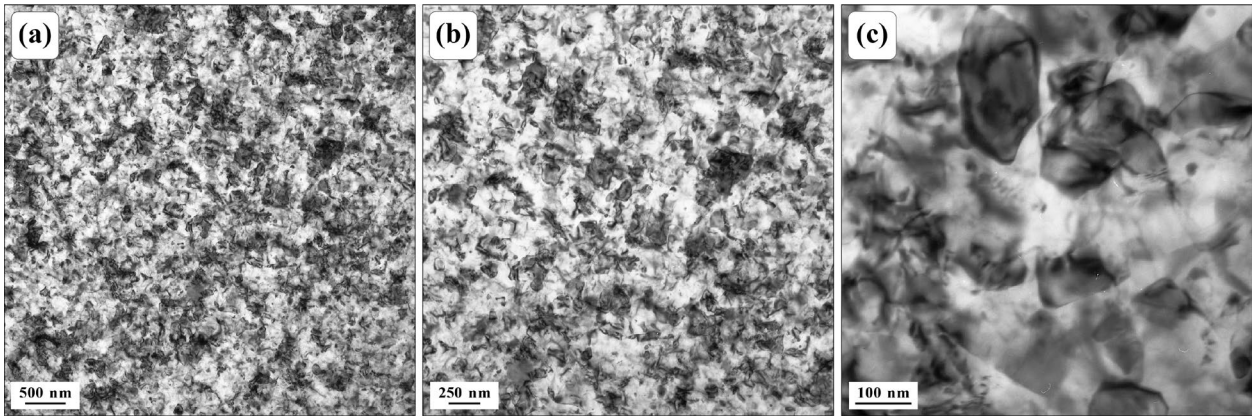
Figure 4. TEM structures of the alloy 1570C after MIF1+HPT processing

3.2. Microhardness and tensile properties

The alloys microhardness and the tensile strength after the proposed MIF-based TMP (Table 2) show a good correlation with the deformation-induced changes in the microstructure (c.f. Figs. 1-4), which holds particularly well when the alloy strengthening was controlled by the dislocation density. The less usual trends were found with regard to the grain size effect. Indeed, the fine-grained MIF1 alloy exhibits the microhardness, yield stress and ultimate tensile strength comparable or even smaller than those in the as-cast specimens, albeit with remarkably higher ductility. These findings could be rationalised in terms of the deformation-induced softening caused by the coagulation of TM aluminides under straining and inter-cycle annealing (Figs. 2c and 3d). This process occurs concurrently with the development of the nearly completely recrystallised equilibrium grain structure with the low dislocation density, giving rise to the small, but not negligible, work hardening effect, and enhancing alloy ductility. Thus, the high-temperature MIF1 processing did not result in the alloy strengthening despite the substantial grain refinement. This observation highlights the significance of apparent softening associated with the reduced dispersion hardening compromising the grain boundary strengthening. Comparing these findings with the data reported in the previous studies (c.f. [6, 47]), the hardening-softening dualism appears to be quite common for the different deformation processing routes applied to wrought aluminium alloy with TM additions. The dichotomy and trade-off between these two processes is typical of high-temperature manufacturing.

Table 2. Average grain size and tensile properties of the alloy 1570C at room temperature

Condition	Size of fine grains, d (μm)	Vickers Micro-hardness, HV	Yield Stress, $\sigma_{0.2}$ (MPa)	Ultimate Tensile Strength, σ_{UTS} (MPa)	Elongation to failure, ε_f (%)
Cast	25±5*	105±10	240±10	355±10	27±2
MIF1	2.0±0.2*	105±5	230±5	355±5	38±3
MIF3	1.0±0.2*	125±5	315±10	385±10	32±3
MIF1+CR	-	162±6	460±10	520±15	15±2
MIF1+HPT	0.15±0.05**	240±5	-	800±30	0

* EBSD data

** TEM data

Following the initial MIF1 processing steps, the further forging at the lower temperature was accompanied by the remarkable increase in the alloy strength (c.f. the MIF3 state, Table 2). Particularly, the yield stress and the ultimate tensile strength benefited from the additional deformation, whereas the ductility compromised only slightly. This behaviour was reasonably expected due to the fabrication of the non-equilibrium UFG microstructure with smaller grain/subgrain dimensions, higher dislocation densities and β-phase precipitates (Figs. 1g-i and 3b, e). Whereas the contribution of grain refinement and strain hardening is evident during deformation processing at reduced temperatures, the dispersion hardening caused by the decomposition of the Mg-rich aluminium solid solution and the β-phases formation under straining below the solvus point can be insignificant. The similar finding has been reported in [48] for SPD-manufactured commercial Al-Mg alloys where the dispersion hardening was only able to compensate for the loss in the solid solution strengthening and did not cause any additional strengthening.

The even higher alloy strengthening was obtained under CR of the MIF1 processed billet where the very high monotonic strength (of 520 MPa on average[2]) properties are paired with considerable ductility. Not only this strength-ductility balance is unique for Al-Mg commercial alloys, but, to the best of our knowledge, it is superior to most of the aluminium products in general. Indeed, the MIF1+CR fabricated sheet demonstrates the ultimate tensile strength in excess of 500 MPa. The similar strength is observed in the high-strength age-hardenable 7xxx series Al alloys [49,50], albeit with notably lower ductility in the peak-aged T6 condition, c.f. Table 4.

The most work-hardened and dispersed microstructure of the matrix was obtained after HPT following MIF1 processing. In that case, the alloy strengthening was controlled by two main factors - grain refinement down to the nanoscale and the formation of the non-equilibrium microstructure with a high density of lattice defects (Fig. 4 and Tables 1 and 2). However, the extraordinary alloy strengthening was obtained at the expense of ductility, which was virtually nullified, making this way of extreme strength enhancement impractical.

3.3. Fatigue resistance

As has been discussed above, the alloy 1570C processed via different SPD-based TMP routes exhibits notably different microstructures and, therefore, different resultant tensile properties. The significant strengthening effect observed in the MIF1+CR state brings some optimism to the prospects of improving the fatigue resistance as well since the conventional fatigue limit is often, though admittedly not always, correlates with the ultimate tensile strength in many structural materials [51] including light metals and alloys [26].

Figure 5 shows the fatigue Wöhller plots in terms of the number of cycles to failure corresponding to the maximum applied cyclic stress σ_{max} at chosen R=0.1 (S-N) in a log-log scale. The significant scatter of experimental data, which is particularly noteworthy for the as-cast and MIF1+HPT alloys, is associated with the sub-size specimen dimensions making the testing specimens vulnerable to the surface quality, localised stress risers and microstructural

---

[2] We should note here that the peak σ_{UTS} value for the MIF1+CR state was obtained at 570 MPa. However, since this value was too far away from the mean observed in the main series of experiments, it was treated as outlier and not included in the calculations of confidence intervals shown in Table 2.

inhomogeneities intimately inherited from processing. While in the as-cast material, the scatter can be related to the inherent faultiness and inhomogeneity of the as-cast structure, the microcracks, which are frequently introduced by HPT in the high-strength materials can be responsible for the fluctuations in the experimentally measured fatigue life. Typically for many nonferrous metals and alloys, the Al-Mg-TM alloy tested does not exhibit a well-defined endurance limit. In log-log coordinates, the S-N data can be reasonably approximated by straight lines without a clear transition between low- and high-cycle regimes. In other words, the experimentally measured stress-life data, Fig. 5, reasonably follow the Basquin-type decay according to the power relationship of the general form

$$\sigma_{max} = A\left(2N_f\right)^b \tag{1}$$

where A and b are the structurally-sensitive material parameters: A is related to the fatigue strength coefficient, and b is known as the fatigue strength exponent, respectively.

Using the linear regression analysis, the mean conventional fatigue limits $\sigma_{f0.1}$ have been estimated at 4×10^6 number of cycles to failure N_f at R=0.1 and listed in Table 3 in terms of the peak stress applied during the loading session. Basquin parameters A and b, which are commonly sued to characterise fatigue life, are also shown for comparison.

The highest fatigue resistance across all alloy conditions tested was demonstrated by the MIF1+CR processed specimens having the UFG work-hardened microstructure resulting in the best balance between the tensile strength and ductility (Table 2). The shortest fatigue life was recorded for the reference as-cast alloy. Compared to MIF-processed specimens, the MIF+HPT-superstrengthened and nanostructured alloy showed a lower average endurance over the entire investigated range of applied stress amplitudes in both low- and high-cycle fatigue domains. Let us notice that the shorter fatigue life was observed despite the impressive monotonic strength exceeding 800 MPa obtained in the MIF+HPT processed alloy. The fractographic analysis corroborates the results of the tensile testing and suggests that it is the brittleness and the high sensitivity to stress concentrators (Fig, 6a-c) that is responsible for this effect in the extremely strengthened alloy. Two factors can be considered important for the shorter than expected fatigue life in the HPT processed specimens: (i) microcracks or other significant local stress risers induced coincidentally during low-temperature SPD processing and facilitating premature crack initiation at the specimen's surface, and (ii) poor resistance to fatigue crack propagation in the severely work-hardened nanocrystalline matrix as is frequently reported for the fatigue crack growth in SPD-processed metals and alloys [52-55]. Both arguments are backed by the fractographic observations revealing multiple sites of fatigue crack nucleation (Fig. 6a) and the brittle mode of fatigue crack propagation resulting in the nearly flat fracture surface after HPT (Fig. 6a-c). Nonetheless, a noteworthy result is that at least one specimen in this series did not break at the 320 MPa peak stress up to 4×10^6 loading cycles, thus showing the principal possibility to achieve an exceptionally long fatigue life in the nanostructured materials at high stresses.

The fatigued as-cast specimen exhibits the fracture surface with the single initiation site at the specimen's edge (Fig. 6d). The well-defined stable crack growth zone revealing the intercrystalline fatigue crack path is clearly visible (Fig. 6e) before final rupture occurred in a ductile mode (Fig. 6f).

The MIF-based SPD processing accompanied by significant grain refinement and the development of excellent microstructural homogeneity in the recrystallised ultrafine structures

results in the considerable increase in the fatigue limit concomitantly with the increase in the monotonic strength as compared to the reference as-cast specimens. The fatigue fracture surface after MIF1 processing exhibits the notably more significant roughness with the pronounced ductile features prevailing along the crack path (c.f. Fig. 6g, h and i; the fatigue beach markings reveal the successive positions of the advancing crack front, Fig. 6g). The microcracks did not appear on the fracture surface, whereas the ductile dimples are omnipresent. Hence, compared to the as-cast material, the fatigue fracture mode changed from brittle to ductile, which implies a greater involvement of plasticity and greater mechanical work spent on the formation of free surfaces during crack propagation. It is particularly noteworthy that the fatigue toughness increased after MIF processing, which, as has been repeatedly discussed in the literature, is not frequently seen in many SPD-fabricated alloys, and this should be ascribed to the collective effect of the grain/subgrain refinement and the redistribution of strengthening phases - precipitates of TM aluminides and the β-phase – leading to the improved uniformity in the microstructure (Figs. 3 and 4).

The cold-rolling following the MIF1 procedure did not qualitatively change the fatigue fracture mode. The fracture surface appearance could still be regarded as ductile, even though, in contrast to the MIF states, no fatigue beach markings or striations were evident on the fracture surface (Fig. 6j, k). The layered-like surface relief was formed along the crack path, which was likely correlated with the pancaked grain structure created by rolling. It is interesting to notice that such an ultrafine-grained, layered and highly deformed microstructure with high densities of TM aluminides has, however, enabled a high resistance to crack propagation. The crack growth occurred across the layers and was accompanied by fine secondary cracks appearing along the crack path. The final rupture also occurred in a ductile manner with clearly visible fine dimples (Fig. 6 l) that also correlated with the overall high ductility of the processed alloy and its high fracture toughness.

Due to the specimen size limitations, cyclic experiments have been performed in the tension-tension mode at R=0.1. The tensile mean stresses $\sigma_m = \frac{1}{2}\left(\sigma_{max} + \sigma_{min}\right) = \frac{\sigma_{max}}{2}\left(1 + R\right)$ exert significant influence on fatigue resistance: they promote fatigue crack initiation and accelerate crack growth, thus shortening fatigue life. To account for the mean stress effect on fatigue life in the high-cycle regime, many models have been proposed in conjunction with the stress-based approach. The commonly used empirical models, such as those by Goodman, Gerber, Morrow, Walker, and Smith, Watson and Topper (SWT), have been critically reviewed and compared by Dowling [56]. The corollary from the detailed statistical analysis performed in [56] is that the non-parametric SWT equation

$$\sigma_{ar} = \sqrt{\sigma_{max}\sigma_a} = \sigma_{max}\sqrt{\frac{1-R}{2}} \tag{2}$$

yields acceptable, consistent and conservative results for a wide range of materials, and it is shown particularly accurate for middle- and high-strength aluminium alloys in the 2xxx and 7xxx series. Here $\sigma_a = \left(\sigma_{max} - \sigma_{min}\right)/2$ denotes the stress amplitude, and σ_{ar} refers to the equivalent fully reversed stress amplitude resulting in the same fatigue life as the $\sigma_a - \sigma_m$ combination. Therefore, the SWT equation (2) was employed in the present work for the mean stress correction to enable a reasonable comparison of the obtained estimates of the fatigue limit with the findings published elsewhere for similar alloys (Table 4). One should bear

in mind, that the stress-based version of the STW equation can be applied reasonably well only as long as the elastic strain component dominates in the hysteresis loop, i.e. when the stress amplitudes are small enough minimise, if not to eliminate, the plasticity effects. Since the applied peak stresses varied broadly, often exceeding the conventional yield stress, we shall confine ourselves to the lower bounds on the applied stresses to evaluate approximately the fatigue limit in the fully reversed uniaxial stress state. Results of the application of the SWT correction are shown in Table 4 in terms of the anticipated fully reversed conventional fatigue limit σ_{f-1} and can be compared to $\sigma_{f0.1}$.

One can notice that as it is typically observed for many structural materials, the *A* value in the Basquin-type Eq. (1) correlates positively with the measures of a materials resistance to monotonic deformation, e.g. with the ultimate tensile strength σ_{UTS} [26, 57]. The absolute value of the fatigue strength exponent obtained from the least square linear regression (Fig. 6, Table 3) is the lowest for the as-cast alloy b=-0.025 and is ranged in a narrow interval between -0.044 and -0.050 for the SPD-processed conditions. Considering the scattering of the experimental data, the differences among the *b*-values in the deformation processed specimens can be said insignificant. The increase of the Basqiun exponent after deformation processing, including SPD, has been frequently reported in the literature, e.g. [58-60], and this is associated with the strengthening effect, which tends to increase the susceptibility of the material to the internal imperfections inherited from SPD as well as to cyclically induced damage. Thus, compared to the as-cast state, the deformation processing increases the fatigue strength coefficient *A* in parallel with the microstructure refinement and the increasing monotonic strength. Concurrently, the absolute value of the fatigue strength exponent increases by a factor of two or so to approximately 0.045 on average, regardless of the processing modes tested. Taking *b* as an integral fatigue damage parameter, the smaller (more negative) *b*, the greater the cyclically induced damage and the shorter the fatigue life at the same *A*. The highest absolute *b* value and the shorter fatigue life observed in the MIF1+HPT processed alloy is thus plausibly understood. The alloy fabricated via the MIF1 process showed the least scatter of the data points due to the exceptional homogeneity of its equiaxed microstructure with nearly random crystallographic texture, thus illustrating the critical advantage of the MIF processing.

As has been stated above, the CR material demonstrates the overall best fatigue resistance in both low-and high-cycle domains with the peak stress characterising the endurance at R=0.1 and 4×10^6 cycles of 275 MPa and the estimated stress amplitude in the fully reverenced loading with R=-1 of 194 MPa. Even though the latter estimate can be regarded as approximate, the result is remarkable, since the observed fatigue limit appears to be by far superior to other findings reported in the literature for differently manufactured alloys of the similar Al-Mg-TM class, as well as for several popular heat-treatable alloys, c.f. those listed in Table 4. Admittedly, the accurate quantitative comparison of the fatigue results compiled in Table 4 is difficult due to the differences in the specimen's geometry and loading conditions. For example, the data in [37, 64] were collected in the cantilever rotating-beam mode testing, which usually generates the overestimated results on fatigue life if compared to the fully symmetrical push-pull axial loading. Nonetheless, the highest monotonic tensile strength paired with good ductility obtained in the present work for the MIF1+CR manufactured alloy is undeniably favourable. This corroborates the conclusion that the fatigue resistance achieved in the MIF1+CR specimens in the stress-controlled high-cycle regime is also superior when compared to existing data.
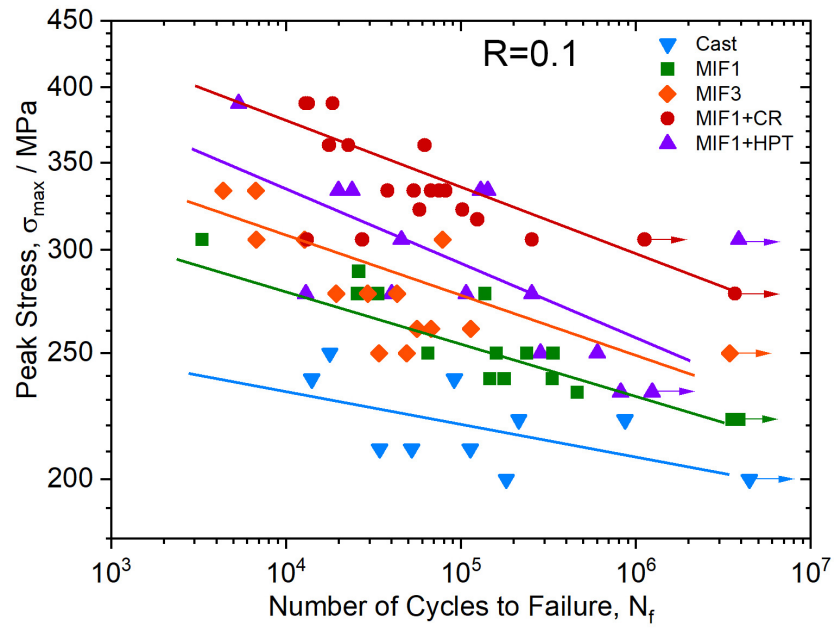
Figure 5. S-N plots of the alloy 1570C processed via different routes. Solid lines represent the results of the least square linear regression used to determine the *b*-exponents

Table 3. Fatigue properties of the alloy 1570C at ambient temperature

Condition	Fatigue Limit, R=0.1 $\sigma_{f0.1}$ (MPa)	Fatigue Limit in reversed loading, R=-1 * σ_{f-1} (MPa)	Fatigue Ratio, $\sigma_{f-1}/\sigma_{UTS}$	Basquin parameters, R=0.1	
				Fatigue strength coefficient, A (MPa)	Fatigue strength exponent, b
Cast	200	134	0.38	295	-0.025
MIF1	215	152	0.42	449	-0.048
MIF3	225	160	0.41	445	-0.044
MIF1+CR	275	194	0.38	550	-0.045
MIF1+HPT	240	170	0.18	525	-0.050

Fatigue limits $\sigma_{f0.1}$ and σ_{f-1} are given in terms of stress amplitudes at 4×10^6 cycles
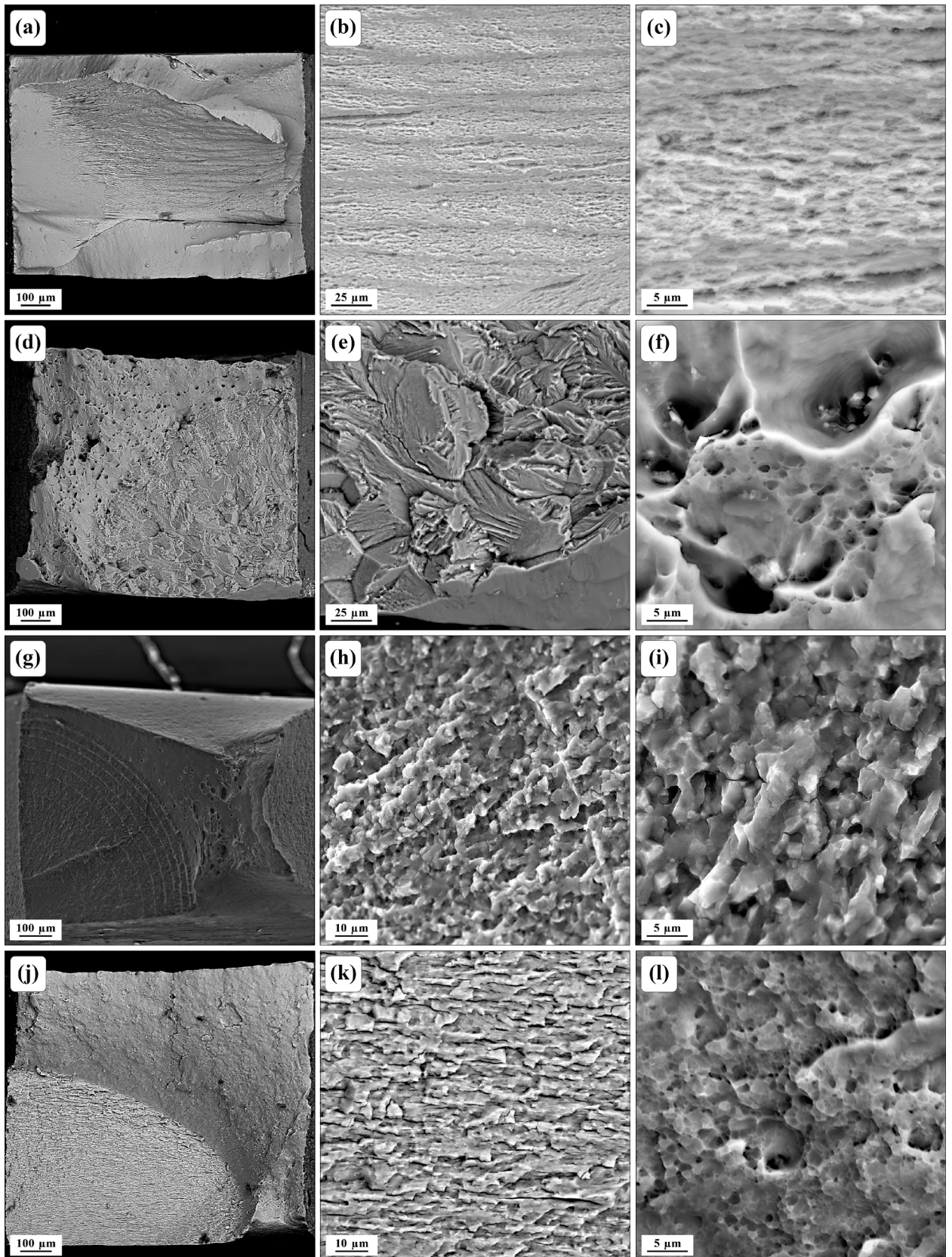* Smith-Watson-Topper corrected for the mean stress

Figure 6. SEM images of the ruptured near the conventional fatigue limit samples the alloy 1570C after MIF1+HPT (a, b, c), as-cast (d, e, f), MIF1-processed (g, h, i) and MIF1+CR (j, k, l); (a, d, g, j) – low magnification images representing the overview of the fatigue fracture, (b, e, h, k) – a magnified view of the fatigue zone near the crack initiation site, (c, i) – intermediate zone of the stable crack growth, (f, l) – rupture zone.

Table 4. Tensile and fatigue properties of differently manufactured Al-Mg-TM alloys in comparison with those for popular commercial alloys

Alloy	Processing	Effective strain	Yield Stress, $\sigma_{0.2}$ (MPa)	Ultimate Tensile Strength, σ_{UTS} (MPa)	Elongation at break, ε_f (%)	Stress Ratio, R	Fatigue Limit, σ_f (MPa)	Fatigue Ratio, σ_f/σ_{UTS}	Ref.
Al-1Mg-0.27Sc	H 632°C+Q		143	211	31	-1	65	0.31	[38]
Al-5.18Mg-0.32Mn-0.25Sc	Hot rolled +A 325°C/1h		240	375	29	-1	150	0.40	[61]
Al-5.7Mg-0.4Mn-0.32Sc	H 520°C/48+E390°C+ A 400°C/1h+ECAP 325°C (8C passes)	8	274	388	22.2	-1*	180	0.45	[37]
Al-6Mg-0.2Sc-0.15Zr	H 420°C+ ECAP320°C (4Bc passes)	4.6	230	410	29	-1	150	0.36	[34]
Al-6.2Mg-0.45Mn-0.24Sc-0.08Zr	H530°C+Q+ECAP220°C (6Bc passes)	6.8	320	428	13.4	0.1	150	0.35	[62]
Al-6Mg-0.35Mn-0.20Sc-0.08Zr-0.07Cr	H360C/12h+ECAP 320°C (12 Bc passes)	12	365	440	22	0.1	195	0.44	[63]
Al-5Mg-0.18Mn-0.20Sc-0.08Zr	H360°C for 6 h, MIF1 325°C + CR	13.6	460	520	15	0.1 -1**	275 190	0.36	Present work
2024-T4	-	-	325	470	20	-1*	140	0.30	[64]
6061-T6	-	-	275	315	12	-1*	95	0.30	[64]
7075-T6	-	-	500	570	11	-1*	160	0.28	[64]

H -homogenisation, A -annealing, Q - quenching in water, E -extrusion

* Rotating bending

** SWT-corrected

4. Conclusions

1) The hot MIF processing of the homogenised billet of the complex Al-Mg-TM alloy resulted in the insignificant effect on the strength properties assessed in monotonic tension despite significant grain size reduction down to the submicrocrystalline range. The Hall-Petch strengthening was compromised by the partial loss in the dispersion strengthening effect due to TM aluminides coarsening;

2) The multistep MIF processing performed with the inter-step temperature reduction produced the more refined and strain-hardened UFG structure consisting of the nearly equiaxed grains/subgrains with the high dislocation density and weak metallographic texture, which, overall, resulted in the substantial strengthening effect at monotonic loading with only the slightly compromised ductility.

3) The fatigue behaviour of the alloy with the UFG or nanocrystalline structures formed in the course of the thermomechanical processing combining hot MIF with cold straining via rolling or high-pressure torsion follows the common trends in the fatigue life approach: the positive correlation between the ultimate tensile strength and the fatigue resistance in the high-cycle regime is seen.

4) The MIF process followed by cold-rolling is shown to be capable of producing the sheets with the uniform ultrafine grain structure and an outstanding combination of the high strength exceeding 500 MPa, elongation at break greater than 15% in monotonic tension, and fatigue endurance at R=0.1 or -1 superior to that in other alloys of the same class of non-heat treatable Al-Mg-TM systems or even many popular commercial heat-treatable alloys, thus demonstrating the critical advantages of the proposed processing route for fabricating the sizable UFG semi-finished products with excellent properties.

Data availability. The experimental data are available from the corresponding author upon reasonable request.

References

[1] Y. Filatov, V. Elagin, V. Zakharov, New Al–Mg–Sc alloys, Mater. Sci. Eng. A 280 (1) (2000) 97-101.

[2] E. Avtokratova, O. Sitdikov, M. Markushev, R. Mulyukov, Extraordinary high-strain rate superplasticity of severely deformed Al-Mg-Sc-Zr alloy, Mater. Sc.i Eng. A 538 (2012) 386-390. doi:10.1016/j.msea.2012.01.041.

[3] O. Sitdikov, R. Garipova, E. Avtokratova, O. Mukhametdinova, M. Markushev, Effect of temperature of isothermal multidirectional forging on microstructure development in the

Al-Mg alloy with nano-size aluminides of Sc and Zr, J. Alloys Compd. 276 (2018) 520-531. doi:10.1016/j.jallcom.2018.02.277.

[4]   R. Valiev, T. Langdon, Principles of equal-channel angular pressing as a processing tool for grain refinement, Prog. Mater. Sci. 51 (2006) 881-981. doi:10.1016/j.pmatsci.2006.02.003.

[5]   A. Vinogradov, Y. Estrin, Extreme grain refinement by severe plastic deformation: A wealth of challenging science, Acta Mater. 61 (2013) 782-817. doi: 10.1016/j.actamat.2012.10.038.

[6]   E. Avtokratova, O. Sitdikov, O. Mukhametdinova, M. Markushev, S.V.S.N. Murty, M.J.N.V Prasad, B.P. Kashyap, Microstructural evolution in Al–Mg–Sc–Zr alloy during severe plastic deformation and annealing, J. Alloys Compd. 673 (2016) 182-194. doi:10.1016/j.jallcom.2016.02.207.

[7]   R.R. Mulyukov, R.M. Imayev, A.A. Nazarov, M.F. Imayev, V.M. Imayev, Superplasticity of Ultrafine Grained Alloys: Experiment, Theory, Technologies, Nauka, Moscow, 2014 (in Russian).

[8]   M. Markushev, E. Avtokratova, S. Krymskiy, O. Sitdikov, Effect of Precipitates on Nanostructuring and Strengthening of High-strength Aluminum Alloys Under High Pressure Torsion, J. Alloys Compd. 743 (2018) 773-779. doi:10.1016/j.jallcom.2018.02.047.

[9]   O. Sitdikov, S. Krymskiy, M. Markushev, E. Avtokratova, T. Sakai, Effect of heat treatment on nanostructuring in high-strength aluminum alloy by severe plastic deformation, Rev. Adv. Mater. Sci. 31 (2012) 62-67.

[10]   V. Segal, Materials Processing by Simple Shear, Mater. Sci. Eng. 197 (1995) 157–164. doi: 10.1016/0921-5093(95)09705-8

[11]   A. Gholinia, P. Prangnell, M. Markushev, The effect of strain path on the development of deformation structures in severely deformed aluminum alloys processed by ECAE, Acta Mater. 48 (5) (2000) 1115–1130. doi:10.1016/S1359-6454(99)00388-2

[12]   F. Humphreys, P. Prangnell, J. Bowen, A. Gholinia, C. Harris, Development of stable fine-grain structures by large strain deformation, Trans. Roy. Soc. A 357 (1999) 1663–1680.

[13]   M. Markushev, On the effectiveness of some methods of severe plastic deformation for bulk nanomaterials processing, Letters on Mater. 1 (1) (2011) 36-42. doi:10.22226/2410-3535-2011-1-36-42.

[14]   R.W. Armstrong, N. Balasubramanian, Unified Hall-Petch description of nano-grain nickel hardness, flow stress and strain rate sensitivity measurements, AIP Advances 7(8) (2017) 085010. https://doi.org/10.1063/1.4996294

[15]   A. Vinogradov, Y. Estrin, Analytical and numerical approaches to modelling severe plastic deformation, Prog. Mater. Sci. 95 (2018) 172-242. doi: 10.1016/j.pmatsci.2018.02.001.

[16]   H. Mughrabi, Fatigue, an everlasting materials problem - still en vogue, Procedia Eng. 2 (1) (2010) 3-26. https://doi.org/10.1016/j.proeng.2010.03.003.

[17]   HW Höppel, H Mughrabi, A Vinogradov, Fatigue properties of bulk nanostructured materials, in Bulk Nanostructured Materials; Zehetbauer, MJ, Zhu, YT, Eds.; WILEY-VCH Verlag GmbH & Co. KGaA, Weinheim, Germany, 2009.

[18]   H. Mughrabi, H.W. Höppel, Cyclic deformation and fatigue properties of very fine-grained metals and alloys, Int. J. Fatigue 32 (9) (2010) 1413-1427. doi:10.1016/j.ijfatigue.2009.10.007.

[19]   V. Patlan, A. Vinogradov, K. Higashi, K. Kitagawa, Overview of fatigue properties of fine grain 5056 Al-Mg alloy processed by equal-channel angular pressing, Mater. Sci. Eng. A 300(1-2) (2001) 171-182. doi: 10.1016/S0921-5093(00)01682-8

[20]   V. Patlan, K. Higashi, K. Kitagawa, A. Vinogradov, M. Kawazoe, Cyclic response of fine grain 5056 Al-Mg alloy processed by equal-channel angular pressing, Mater. Sci. Eng. A 319 (2001) 587-591.

[21]   C.Y. Yu, P.L. Sun, P.W. Kao, C.P. Chang, Mechanical properties of submicron-grained aluminium, Scripta Mater. 52 (5) (2005) 359-363. doi:10.1016/j.scriptamat.2004.10.035.

[22]   D.R. Fang, Z.F. Zhang, S.D. Wu, C.X. Huang, H. Zhang, N.Q. Zhao, J.J. Li, Effect of equal channel angular pressing on tensile properties and fracture modes of casting Al–Cu alloys, Mater. Sci. Eng. A 426 (1-2) (2006) 305-313. doi:10.1016/j.msea.2006.04.044.

[23]   T. Huang, L. Shuai, A. Wakeel, G. Wu, N. Hansen, X. Huang, Strengthening mechanisms and Hall-Petch stress of ultrafine grained Al-0.3%Cu, Acta Mater. 156 (2018) 369-378. doi: 10.1016/j.actamat.2018.07.006.

[24]   N. Tsuji, Y. Ito, Y. Saito, Y. Minamino, Strength and ductility of ultrafine grained aluminum and iron produced by ARB and annealing, Scripta Mater. 47 (12) (2002) 893-899. doi: 10.1016/S1359-6462(02)00282-8

[25]   H.W. Höppel, H. Mughrabi, A. Vinogradov, Fatigue Properties of Bulk Nanostructured Materials, Wiley-VCH Verlag GmbH & Co. KGaA, Weinheim, 2009.

[26]   Y. Estrin, A. Vinogradov, Fatigue behaviour of light alloys with ultrafine grain structure produced by severe plastic deformation: An overview, Int. J. Fatigue 32 (6) (2010) 898-907. doi: 10.1016/j.ijfatigue.2009.06.022.

[27]   V.I. Elagin, V.V. Zakharov, T.D. Rostova, Scandium-alloyed aluminum alloys, Metal Sci. Heat Treat. 34(1) (1992) 37-45 https://doi.org/10.1007/BF00768707.

[28]   J. Royset, N. Ryum, Scandium in aluminium alloys, Int. Mater. Rev. 50(1) (2005) 19-44. doi 10.1179/174328005X14311

[29]   V.V. Zakharov, Effect of Scandium on the Structure and Properties of Aluminum Alloys, Metal Sci. Heat Treat. 45(7) (2003) 246-253

[30]   M.S. Kaiser, S. Datta, A. Roychowdhury, M.K. Banerjee, Effect of scandium additions on the tensile properties of cast Al-6Mg alloys, J. of Materi. Eng. and Perform. 17(6) (2008) 902-907. doi:10.1007/s11665-008-9242-4.

[31]   Y.Y. Li, W.H. Wang, Y.F. Hsu, S. Trong, High-temperature tensile behavior and microstructural evolution of cold-rolled Al-6Mg-0.4Sc-0.13Zr alloy, Mater. Sci. Eng. A 497(1-2) (2008) 10-17. doi:10.1016/j.msea.2008.08.019.

[32]   S.V. Dobatkin, V.V. Zakharov, R.Z. Valiev, A.Y. Vinogradov, T.D. Rostova, N.A. Krasilnikov, E.N. Bastarash, I.B. Trubitsyna, Nano- and Submicrocrystalline Structure Formation during High Pressure Torsion of Al-Sc and Al-Mg-Sc Alloys, in: M. Zehetbauer and R. Z. Valiev (Eds.), Nanomaterials by Severe Plastic Deformation, Wiley-VCH Verlag GmbH & Co. KGaA, Weinheim, 2005, pp. 158-164.

[33]   S. Dobatkin, V. Zakharov, A. Vinogradov, K. Kitagawa, N. Krasil'nikov, T. Rostova, E. Bastarash, Nanocrystalline structure formation in Al-Mg-Sc alloys during severe plastic deformation, Russian Metallurgy (Metally) 2006 (6) (2006) 533-540.

[34]   A. Vinogradov, A. Washikita, K. Kitagawa, V.I. Kopylov, Fatigue life of fine-grain Al-Mg-Sc alloys produced by equal-channel angular pressing, Mater. Sci. Eng. A 349 (1-2) (2003) 318-326. doi:10.1016/S0921-5093(02)00813-4.

[35]   D. Orlov, A. Reshetov, A. Synkov, V. Varyukhin, D. Lotsko, O. Sirko, N. Zakharova, A. Sharovsky, V. Voropaiev, Y. Milman, S. Synkov, Twist Extrusion as a Tool for Grain Refinement in Al-Mg-Sc-Zr Alloys, in: Y.T. Zhu, V. Varyukhin (Eds.), Nanostructured Materials by High-Pressure Severe Plastic Deformation, Springer Netherlands, 2006, pp. 77-82

[36] H. Akamatsu, T. Fujinami, Z. Horita, T.G. Langdon, Influence of rolling on the superplastic behaviour of an Al-Mg-Sc alloy after ECAP, Scripta Mater. 44 (5) (2001) 759-764. doi: 10.1016/S1359-6462(00)00666-7

[37] E.V. Avtokratova, R.O. Kaibyshev, O.S. Sitdikov, Fatigue of a fine-grained high-strength Al-6Mg-Sc alloy produced by equal-channel angular pressing, Phys. Metals Metallogr. 105 (5) (2008) 500-508. doi:10.1134/S0031918X08050116.

[38] C. Watanabe, R. Monzen, K. Tazaki, Effects of Al_3Sc particle size and precipitate-free zones on fatigue behaviour and dislocation structure of an aged Al–Mg–Sc alloy, Int. J. Fatigue 30 (4) (2008) 635-641. doi:10.1016/j.ijfatigue.2007.05.010.

[39] C. Watanabe, R. Monzen, Fatigue behaviour and microstructure of an Al-Mg-Sc alloy at an elevated temperature, Journal of Physics: Conference Series 240 (2010) 012049. doi:10.1088/1742-6596/240/1/012049.

[40] C. Watanabe, C.Y. Jin, R. Monzen, K. Kitagawa, Low-cycle fatigue behaviour and dislocation structure of an Al–Mg–Sc alloy, Mater. Sci. Eng. A 387-389 (2004) 552-555. doi:10.1016/j.msea.2004.05.079.

[41] P.B. Hirsch, A. Howie, R.B. Nicholson, D.W. Pashley, M.J. Whelan, Electron Microscopy of Thin Crystals, Butter Worths, London, 1965.

[42] O.N. Senkov, M.R. Shagiev, S.V. Senkova, D.B. Miracle, Precipitation of Al_3(Sc,Zr) particles in an Al-Zn-Mg-Cu-Sc-Zr alloy during conventional solution heat treatment and its effect on tensile properties, Acta Mater. 56 (2008) 3723-3738. doi:10.1016/j.actamat.2008.04.005

[43] A.G. Mochugovskiy, A.V. Mikhaylovskaya, N.Yu. Tabachkova, V.K. Portnoy, The mechanism of L12 phase precipitation, microstructure and tensile properties of Al-Mg-Er-Zr alloy, Mater. Sci. Eng. A 744 (2019) 195–205.

[44] T. Kobayashi, Strength and fracture of aluminum alloys, Mater. Sci. Eng. A 280(1) (2000) 8-16. doi: 10.1016/S0921-5093(99)00649-8

[45] O. Sitdikov, E. Avtokratova, M. Markushev, Influence of strain rate on grain refinement in the Al-Mg-Sc-Zr alloy during high-temperature multidirectional isothermal forging, Mater. Characterization 157 (2019) 109885. doi:10.1016/j.matchar.2019.109885.

[46] M. Murashkin, A. Kilmametov, R. Valiev, Structure and mechanical properties of an aluminum alloy 1570 subjected to severe plastic deformation by high-pressure torsion, Phys. Metals Metallogr. 106 (2008) 90-96. https://doi.org/10.1134/S0031918X08070120.

[47] E. Avtokratova, O. Sitdikov, O. Latypova, M. Markushev, Effect of the bimodal structure processed by ECAP and subsequent rolling on static strength and superplasticity of Al-Mg-Sc-Zr alloy, Facta Universitatis. Series: Mechanical Engineering 18 (2) (2020) 255 – 267 doi:10.22190/FUME200601023A.

[48] M. Markushev, M. Murashkin, Strength and crack resistance of commercial aluminum alloys 1560 and 5083 of the Al-Mg-Mn system after severe plastic deformation via angular pressing, Phys. Metals Metallogr. 98 (2004) 221-231.

[49] ASM Handbook, Volume 2, Properties and selection: Nonferrous alloys and special-purpose materials, 10th ed., Russell: ASM International, 1990.

[50] L. Katgerman, D. Eskin. Hardening, annealing, and aging In Handbook of aluminium, Volume 1, Physical metallurgy and processes, Marcel Dekker, Inc., NY, U.S.A., 2003.

[51] R.I. Stephens, F. Ali, R.R. Stephens, H.O. Fuchs, Metal fatigue in engineering, second ed., Wiley, New York, 2001.

[52] A. Vinogradov, Fatigue limit and crack growth in ultra-fine grain metals produced by severe plastic deformation, J. Mater. Sci. 42(5) (2007) 1797-1808. doi: 10.1007/s10853-006-0973-z.

[53] P. Cavaliere, Fatigue properties and crack behavior of ultra-fine and nanocrystalline pure metals, Int. J. Fatigue 31(10) (2009) 1476-1489. doi:10.1016/j.ijfatigue.2009.05.004.

[54] L. Meyer, K. Sommer, T. Halle, M. Hockauf, Crack growth in ultrafine-grained AA6063 produced by equal-channel angular pressing, J. Mater. Sci., 43(23) (2008) 7426-7431. doi:10.1007/s10853-008-2725-8.

[55] T. Leitner, A. Hohenwarter, R. Pippan, Fatigue Crack Growth Behavior of Ultrafine-grained Nickel Produced by High Pressure Torsion, Procedia Mater. Sci. 3 (2014) 1044-1049. doi: 10.1016/j.mspro.2014.06.170.

[56] N.E. Dowling, Mean stress effects in stress-life and strain-life fatigue, SAE Techni. Paper., 2004-01-2227, 2004.

[57] S. Suresh, Fatigue of Materials, Cambridge University Press, UK, London, 1991.

[58] A. Vinogradov, M. Maruyama, Y. Kaneko, S. Hashimoto, Effect of dislocation hardening on monotonic and cyclic strength of severely deformed copper, Philos. Mag. 92(6) (2012) 666-689. doi: 10.1080/14786435.2011.630693.

[59] P. Xue, Z. Huang, B. Wang, Y. Tian, W. Wang, B. Xiao, Z. Ma, Intrinsic high cycle fatigue behaviour of ultrafine grained pure Cu with stable structure, Sci. China Mater. 59(7) (2016) 531-537. doi: 10.1007/s40843-016-5068-6.

[60] M.B. Limooei, M. Zandrahimi, R. Ebrahimi, High cycle fatigue behaviour of Al1070 alloy severely deformed by equal channel angular pressing process, Proc. Inst. Mech. Eng. Part L J. Mat. Des. Appl. 232 (6) (2018) 514-519. https://doi.org/10.1177%2F1464420716637214.

[61] O. Roder, T. Wirtz, A. Gysler, G. Lütjering, Fatigue properties of Al-Mg alloys with and without scandium, Mater. Sci. Eng. A 234-236 (1997) 181-184.

[62] V.F. Terentyev, S.V. Dobatkin, V.I. Kopylov, D.V. Prosvirin, N.V. Petrakova, Features of static and cyclic destruction of submicrocrystalline alloy Al-Mg-Sc, Inorg. Mater.: Appl. Res. 5(1) (2014) 6-13. doi: 10.1134/S2075113314010110.

[63] D. Zhemchuzhnikova, R. Kaibyshev, Effect of deformation structure on fatigue behaviour of an Al-Mg-Sc alloy, IOP Conference Series: Mater. Sci. Eng. 63(1) (2014) 012164. doi:10.1088/1757-899X/63/1/012164.

[64] Handbook of Mechanical Alloy Design, G. E. Totten, L. Xie, K. Funatani (Eds.) Marcel Dekker, Inc., NY, U.S.A., 2004